

BANGS AND METEORS FROM THE QUIET COMET 15P/FINLAY

QUAN-ZHI YE (叶泉志)¹, PETER G. BROWN^{1,2}, CHARLES BELL³, XING GAO (高兴)⁴,
MARTIN MAŠEK⁵, AND MAN-TO HUI (许文韬)⁶¹Department of Physics and Astronomy, The University of Western Ontario, London, ON N6A 3K7, Canada; qye22@uwo.ca²Centre for Planetary Science and Exploration, The University of Western Ontario, London, ON N6A 5B8, Canada³Vicksburg Observatory, Vicksburg, MS, USA⁴No. 1 Senior High School of Ürumqi, Ürumqi, Xinjiang, China⁵Institute of Physics Czech Academy of Sciences, Na Slovance 1999/2, 182 21, Praha, Czech Republic⁶Department of Earth, Planetary and Space Sciences, University of California at Los Angeles, 595 Charles Young Drive East, Los Angeles, CA 90095-1567, USA

Received 2015 March 12; accepted 2015 October 21; published 2015 November 17

ABSTRACT

Jupiter-family comet 15P/Finlay has been reportedly quiet in activity for over a century but has harbored two outbursts during its 2014/2015 perihelion passage. Here we present an analysis of these two outbursts using a set of cometary observations. The outbursts took place between 2014 December 15.4–16.0 UT and 2015 January 15.5–16.0 UT as constrained by ground-based and spacecraft observations. We find a characteristic ejection speed of $V_0 = 300\text{--}650\text{ m s}^{-1}$ for the ejecta of the first outburst and $V_0 = 550\text{--}750\text{ m s}^{-1}$ for that of the second outburst using a Monte Carlo dust model. The mass of the ejecta is calculated to be $M_d = (2\text{--}3) \times 10^5\text{ kg}$ for the first outburst and $M_d = (4\text{--}5) \times 10^5\text{ kg}$ for the second outburst, which corresponds to less than 10^{-7} of the nucleus mass. The specific energy of the two outbursts is found to be $(0.3\text{--}2) \times 10^5\text{ J kg}^{-1}$. We also revisit the long-standing puzzle of the nondetection of the hypothetical Finlayid meteor shower by performing a cued search using the 13 yr data from the Canadian Meteor Orbit Radar, which does not reveal any positives. Earth will pass the 2014/2015 outburst ejecta between 2021 October 6 at 22 hr UT and October 7 at 1 hr UT, with a chance for some significant meteor activity in the radio range, which may provide further clues to the Finlayid puzzle. A southerly radiant in the constellation of Ara will favor the observers in the southern tip of Africa.

Key words: comets: individual (15P/Finlay) – meteorites, meteors, meteoroids

1. INTRODUCTION

Small bodies in the inner solar system are historically classified based on their appearance. “Comet” refers to an object with extended appearance and sometimes one or several tails, while “asteroid” refers to an object that is much smaller than the major planets and appears star-like. Classification by orbital dynamics of these bodies shows that the dynamical characteristics of the two groups of objects differ as well: comets usually possess highly elliptical, parabolic, or hyperbolic orbits, while asteroids usually possess more circular orbits.

Bodies that deviate from these trends (i.e., comets in asteroidal orbits, or asteroids in cometary orbits) are of significant interest, as their dynamical evolution and/or physical properties are apparently exceptional. Although the first such outlier was officially recognized no later than 1989 (e.g., the case of 95P/(2060) Chiron; see Meech & Belton 1989), most outliers were not found until recently with the commissioning of a number of near-Earth asteroid searching/follow-up programs. Comet-like objects in asteroid-like orbits, or “active asteroids” (Jewitt 2012), are more straightforward to recognize as a result of their significant morphological change during the transition to a comet-like state, and so the recognition is usually robust. In contrast, their counterparts, asteroid-like objects in cometary orbits (ACOs), owing to their nature, are considerably more difficult to identify. From an orbital perspective, ACOs are most easily interpreted to be comets that have exhausted their volatiles (or have their volatiles permanently buried by their crusts) so that they appear asteroidal, i.e., they become “dormant comets.” However, dynamical studies have shown that a significant fraction of

ACOs could be asteroids leaking out from the main belt that are temporarily residing in comet-like orbits (Tancredi 2014; Fernández & Sosa 2015), therefore complicating the effort of disentangling orbital properties from physical properties of these bodies.

One approach to identifying dormant comets in the ACO population is to look at comets at an intermediate state between active comets and dormant comets, sometimes labeled as comet-asteroid transition objects (CATOs; e.g., Licandro et al. 2007). A handful of such objects have been suggested, such as 107P/(4015) Wilson–Harrington (Ishiguro et al. 2011), 209P/LINEAR (Ye & Wiegert 2014), and (3552) Don Quixote (Mommert et al. 2014). However, these objects are usually faint and produce little dust, presenting a challenge for further investigation of their surface and dust properties.

15P/Finlay, a Jupiter-family comet (JFC), has been reportedly faint and tailless since its discovery in 1886 (Kronk 2004, 2008; Kronk & Meyer 2010). The comet has a small minimum orbit intersection distance (MOID) of 0.0094 AU to Earth’s orbit but has never been associated with any known meteor shower (Beech et al. 1999). Coupled with the fact that 15P/Finlay has shown a systematic decrease of maximum brightness at each perihelion passage in the past century, it has been suggested that the comet is approaching a state of complete dormancy (Kresak & Kresakova 1989).

However, during its current perihelion passage, 15P/Finlay exhibited two outbursts, each producing a parabolic “shell” around the original coma accompanied by a straight, freshly formed “tail” in the anti-sunward direction. This resembles the historic outburst of 17P/Holmes in 2007 (Buzzi et al. 2007) albeit at a much smaller scale. However, it is notable that 17P/Holmes’s outbursts took place at a larger heliocentric distance

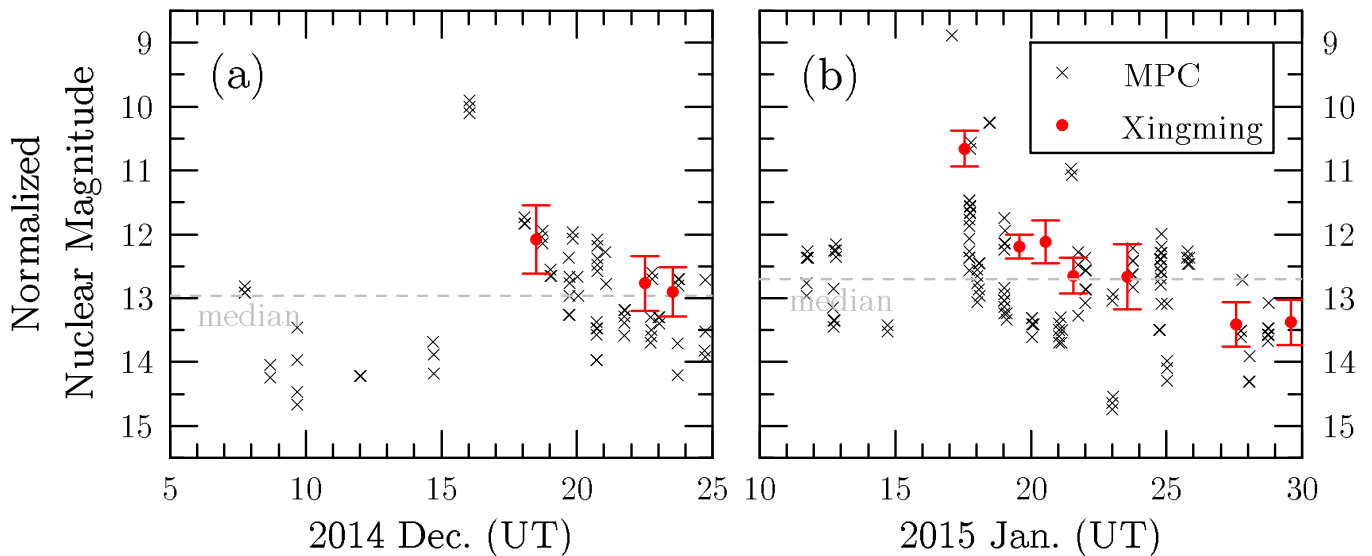


Figure 1. Nucleus magnitude of 15P/Finlay around the time of (a) the first outburst and (b) the second outburst. The Minor Planet Center (MPC) magnitudes (plotted by crosses) are extracted from the Observations Database on the MPC website. The Xingming magnitudes (plotted by red dots) are derived from the monitoring observations by the Xingming 0.35 m telescope with aperture radius $\rho = 5000$ km. The magnitudes are normalized to $\Delta = r_h = 1$ AU assuming a brightening rate $n = 4$ (Everhart 1967).

(2.4 AU) than those of 15P/Finlay (~ 1.0 AU); therefore, the underlying mechanism may not be necessarily the same although the similarity of their overall appearances is striking.

The outbursts of 15P/Finlay are significant in another context: as an Earth-approaching comet, the outburst ejecta may find their way to Earth, creating a meteor outburst. Previously, numerical simulation by Mikhail Maslov⁷ has suggested that the material released in 2014 will have a direct encounter with Earth in 2021, which may produce a meteor outburst with a zenith hourly rate (ZHR) of up to 50. Recent calculation by Mikiya Sato⁸ also arrived at similar results. An outburst from the parent comet may result in a stronger meteor event depending on the ejection velocity and planetary perturbation. Potential meteor observations allow us to directly sample materials from a dormant comet candidate without a dedicated space mission, which may help in understanding the comet itself, as well as the dormant comets as a population. In particular, meteor activity from ACOs can help establish prior periods of activity and constrain the dust production history of ACOs.

In this work, we present an analysis of the observations of 15P/Finlay taken during the two 2014/2015 outbursts. The goal is to understand the underlying nature of the outburst as well as the evolutionary status of the comet. We also examine the yet-to-be-discovered Finlayid meteor shower and especially the potential 2021 meteor outburst. Nondetection of the shower places constraints on the past dust production history of 15P/Finlay.

2. OBSERVATIONS

2.1. Amalgamation of Outburst Reports

The first outburst of 15P/Finlay took place in the late hours of 2014 December 15, the timing being constrained by reports

⁷ <http://feraj.narod.ru/Radiants/Predictions/1901-2100eng/Finlayids1901-2100predeng.html>, accessed 2015 January 17.

⁸ <https://groups.yahoo.com/neo/groups/meteorobs/conversations/messages/44030>, retrieved 2015 March 4.

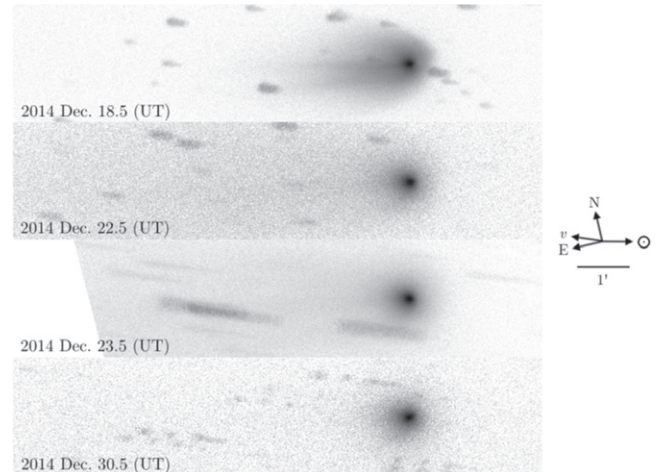


Figure 2. Composite images of 15P/Finlay for the first outburst as observed at Xingming Observatory. The images have been stretched in asinh scale. The scale bar shows the direction to the Sun, the comet’s velocity vector, and the directions of the plane of the sky.

from Christopher Wyatt (Walcha, Australia; December 15.43 UT) and Slooh.com Chile Observatory (La Dehesa, Chile; December 16.04 UT).⁹ During the outburst, the comet brightened by about 3 mag and developed a spiky tail. The tail diluted into the background, with the brightness returning to its normal range by December 21–22 (Figures 1(a) and 2).

The second outburst took place around 2015 January 16.0 UT as noted by Alan Hale (Cloudcroft, NM) at January 16.07, who noted “very bright, almost star-like central condensation” that was absent in the earlier observations.¹⁰ The last negative

⁹ Wyatt’s observation is accessible through the Comet Observation Database (COBS), available at <http://www.cobs.si>; observation from Slooh.com Chile Observatory was published in the Minor Planet Circular No. 90932 (http://www.minorplanetcenter.net/iau/ECS/MPCArchive/2015/MPC_20150105.pdf). Both resources were accessed on 2015 January 17.

¹⁰ <https://groups.yahoo.com/neo/groups/comets-ml/conversations/messages/24322>, accessed on 2015 July 17, as well as private communication with Alan Hale.

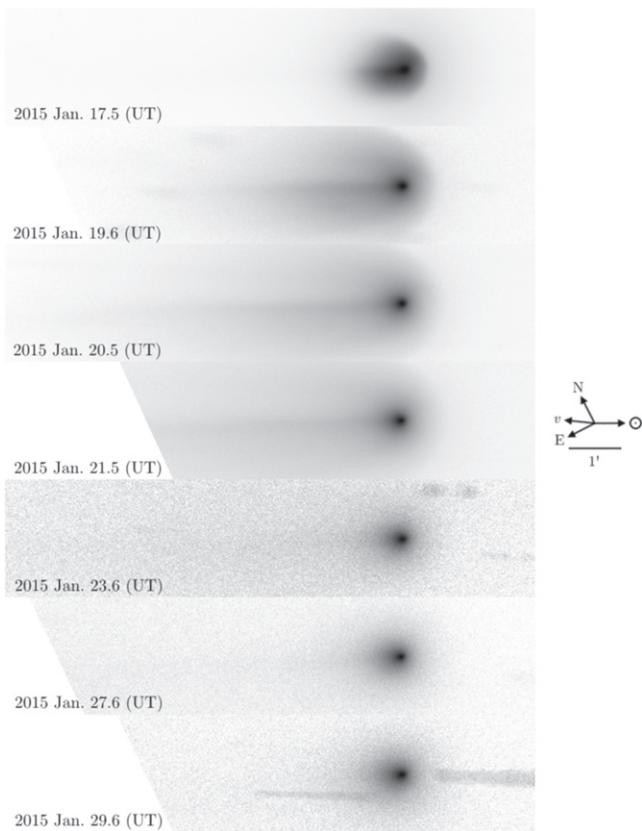


Figure 3. Composite images of 15P/Finlay images for the second outburst as observed at Xingming Observatory. The images have been stretched in asinh scale. The scale bar shows the direction to the Sun, the comet’s velocity vector, and the directions of the plane of the sky.

observation comes from the Solar Wind ANisotropies all-sky hydrogen Ly α camera (SWAN) on board the *Solar and Heliospheric Observatory* (SOHO; Bertaux et al. 1995) around January 15.5 UT.¹¹ The outburst was subsequently noted independently by Guo Zheng-Qiang (Shenyang, China; January 16.43 UT) and Michael Mattiazzo (Swan Hill, Australia; January 16.45 UT)¹², as well as on the SWAN image taken near January 16.5 UT (next-to-last nondetection image). The comet brightened by about 4–5 mag during the second outburst, again with a freshly formed tail. The brightness returned to the normal range around January 20 (Figure 1(b)), but the tail lingered for a few more days until around January 30 (Figure 3).

2.2. Observation and Image Process

After receiving the reports of the outbursts, 15P/Finlay was monitored using the facilities at F(Ph)otometric Robotic Atmospheric Monitor (FRAM) located at Pierre Auger Observatory (Argentina), Xingming Observatory (China), and Vicksburg (U.S.). The FRAM observations were conducted with a 0.3 m f/6.6 telescope equipped with a Kodak KAF-1603ME sensor, which gives a resolution of 0 $''$.93. The Xingming observations were conducted with a 0.35 m f/6.9

telescope with a Kodak KAF-8300 sensor; images are binned by 2, which gives a resolution of 1 $''$.2. The Vicksburg observations were conducted with a 0.3 m f/10 telescope equipped with a Kodak KAF-1600 sensor, which gives a resolution of 1 $''$.87.

The observations at FRAM and Vicksburg are intended for dust modeling, as such they were conducted with a Cousins *R* filter that blocks flux from major cometary gaseous emissions (such as CN, C₂, C₃). The Xingming observations were conducted with wider temporal coverage but without a filter, intended as a continuous monitor of the development of the outburst. Details of the observations are summarized in Table 1. The images are processed using the standard procedure (bias subtraction, dark subtraction, flat division), with plate constants solved using the UCAC 4 catalog (Zacharias et al. 2013). The images are then medianly combined following the motion of the comet.

The composite images from FRAM and Vicksburg are collapsed into a one-dimensional profile. This is necessary as the considerable irregularities of the near-nucleus dust (i.e., localized jets) complicate the modeling work. The orbital plane angles at the two outbursts were also shallow enough ($\sim 4^\circ$) to minimize the information loss during the image collapse. The one-dimensional profile is simply derived from averaging a 2 $'$ wide strip along the Sun-comet axis, with the width of 2 $'$ corresponding to the maximum width of the tail.

3. ANALYSIS

3.1. General Morphology and Evolution of the Outbursts

The composite images from the monitoring observations at Xingming (Figures 2 and 3) show that the morphologies and evolution of both outbursts are comparable: both outbursts produced a newly formed dust shell that is slightly asymmetric with respect to the comet-Sun axis; the dust shell expands as time goes by and fades into the background within ~ 1 week.

We perform aperture photometry with the Xingming data. This is motivated by the considerable scatter shown on the magnitudes provided by the Minor Planet Center (MPC)¹³, possibly owing to different instrumental and measurement settings adopted by different observers. Data from FRAM and Vicksburg are not used at this stage to avoid the complication due to instrumental differences. We use an aperture of $\rho = 5000$ km as projected at the distance of the comet centered at the nucleus. Both 0.35 m and MPC magnitudes are reduced to “normalized” magnitudes at $r_H = \Delta = 1$ AU using $M_N = m_N - 5 \log \Delta - 2.5n \log r_H$, where M_N and m_N are normalized and observed nuclear magnitudes, r_H and Δ are heliocentric and geocentric distances in AU, and $n = 4$ is the canonical brightening rate exponent (Everhart 1967). The photometric calibration is performed using the V-band data from the AAVSO All-sky Photometric Survey (APASS) catalog (Henden et al. 2012) as the Xingming system is most sensitive at V band. As shown in Figure 1, the characteristic outburst decay time (i.e., the time elapsed from the peak of the outburst to the point at which the brightness reaches $1/e$ of the peak brightness) is estimated to be at the order of 1 day.

¹¹ <http://sohowww.nascom.nasa.gov/data/summary/swan/swan-images.html>, accessed on 2015 February 9.

¹² Guo’s observation was posted on <http://www.astronomy.com.cn/bbs/thread-305185-1-1.html> (in Chinese); Mattiazzo’s report was posted on his Facebook page. Both resources were accessed on 2015 January 17.

¹³ Available from the MPC Observations Database, http://www.minorplanetcenter.net/db_search, retrieved 2015 February 3.

Table 1
Summary of the Imaging Observations

Date	Time ^a (UT)	Facility ^b	Total Exposure (minutes)	Filter	r_H (AU)	Δ (AU)	Plane Angle
2014 Dec 17	00:57	FRAM	8	R_C	0.987	1.472	4°3
2014 Dec 18	00:57	FRAM	8	R_C	0.985	1.467	4°3
2014 Dec 18	12:01	Xingming	10	Unfiltered	0.984	1.465	4°3
2014 Dec 22	12:10	Xingming	24	Unfiltered	0.978	1.446	4°5
2014 Dec 23	12:18	Xingming	51	Unfiltered	0.977	1.442	4°5
2014 Dec 30	12:20	Xingming	26	Unfiltered	0.977	1.416	4°7
2015 Jan 17	12:43	Xingming	83	Unfiltered	1.025	1.394	4°7
2015 Jan 18	00:30	Vicksburg	3	R_C	1.023	1.393	4°7
2015 Jan 19	00:18	Vicksburg	6	R_C	1.028	1.395	4°6
2015 Jan 19	13:41	Xingming	16	Unfiltered	1.035	1.396	4°6
2015 Jan 20	12:53	Xingming	91	Unfiltered	1.040	1.397	4°6
2015 Jan 21	00:44	Vicksburg	6	R_C	1.042	1.398	4°7
2015 Jan 21	13:13	Xingming	88	Unfiltered	1.045	1.399	4°6
2015 Jan 23	13:29	Xingming	17	Unfiltered	1.055	1.403	4°6
2015 Jan 27	13:19	Xingming	88	Unfiltered	1.078	1.415	4°3
2015 Jan 29	13:32	Xingming	68	Unfiltered	1.091	1.422	4°2

3.2. Dust Model and Kinematics of the Ejecta

To understand the dust produced by the outburst event, we model the observations using a Monte Carlo dust model developed in our earlier works (e.g., Ye & Hui 2014; Ye et al. 2016).

The dynamical evolution of the cometary dust is controlled by the ratio between radiation pressure and solar gravity, $\beta_{\text{rp}} = 5.7 \times 10^{-4} / (\rho_d a_d)$, where ρ_d is the bulk density of the dust and a_d the diameter of the dust, both in SI units (Wyatt & Whipple 1950), as well as the initial ejection velocity of the dust. The latter is defined as

$$v_{\text{ej}} = V_0 \beta_{\text{rp}}^{1/2} \cdot \nu, \quad (1)$$

where V_0 is the mean ejection speed of a dust particle of $\beta_{\text{rp}} = 1$ and ν follows a Gaussian probability density function:

$$P(\nu) = \mathcal{N}(1, \sigma_\nu^2), \quad (2)$$

where σ_ν is the standard deviation of ν , used to account for the physical spread ν due to the shape of the dust. In this work we use $\sigma_\nu = 0.3$ following exploration by, e.g., Ishiguro et al. (2014), Jewitt et al. (2014), and Ye et al. (2016).

We assume that the dust size follows a simple power law with a differential size index of q , and that the observed flux is solely contributed by scattered light from the dust particles. Hence, the dust production rate is expressed as

$$N(r_H, a_d) da_d = N_0 \left(\frac{a_d}{1 \mu\text{m}} \right)^{-q} da_d, \quad (3)$$

where N_0 is the mean dust production rate of $1 \mu\text{m}$ particles.

Simulated particles are symmetrically released from the nucleus. For both outbursts, two possible outburst epochs are tested, each corresponding to either the epochs of the last negative (non-outburst) report or the first positive report. For the first outburst, outburst epochs of 2014 December 15.4 UT (as indicated by Wyatt's negative report) and 16.0 UT (indicated by Slooh.com's positive report) are tested; for the second outburst, outburst epochs of 2015 January 15.5 UT (indicated by SOHO/SWAN's negative report) and 16.0 UT (indicated by Hale's positive report) are tested. The production

rate peaks at the outburst epoch and decays exponentially at a characteristic time of 1 day as discussed in Section 3.1.

The size distribution is set to the interval of $\beta_{\text{rp,max}} = 1$ to an upper size limit constrained by the escape speed $v_{\text{esc}} = \sqrt{2GM_N/R_G}$, where $M_N = \frac{4}{3}\pi R_N^3 \rho_N$ is the total mass of the nucleus, $\rho_N = 500 \text{ kg m}^{-3}$ the bulk density of the nucleus, $R_N = 0.92 \text{ km}$ the effective nucleus radius (Fernández et al. 2013), and $R_G = 10R_N$ the characteristic distance at which gas drag becomes negligible (Gombosi et al. 1986). We only consider $\beta_{\text{rp,max}} = 1$ because (1) optical observations are most sensitive to $\beta_{\text{rp}} \sim 1$ (micron-sized) particles; (2) larger particles stay closer to the nucleus (as gravitational force dominates), and models with $\beta_{\text{rp,max}} \ll 1$ are incompatible with the observations as they are not able to reproduce the obscured extended dust tails; and (3) complications arise for the dynamics of $\beta_{\text{rp,max}} \gg 1$ (submicron-sized) particles as these are also subjected to Lorentz forces.

We use the MERCURY6 package (Chambers 1999) to integrate particles from the start epoch (i.e., the outburst epoch) to the observation epoch, using the 15th-order RADAU integrator (Everhart 1985). To accommodate the uncertainty in the exact epoch of the outburst, multiple outburst epochs, cued by the reports discussed in Section 2.1, are tested in the simulation. The production of simulated particles peaks at the assumed outburst epoch and decays exponentially afterward, with a characteristic decay time of 1 day as found earlier in Section 3.1. Gravitational perturbations from the eight major planets (the Earth–Moon system is represented by a single mass at the barycenter of the two bodies), radiation pressure, and Poynting–Robertson effect are included in the integration. 15P/Finlay's orbital elements are extracted from the JPL small-body database elements K085/15 (<http://ssd.jpl.nasa.gov/sbdb.cgi>) as listed in Table 2.

The resulting modeled image is convolved with a two-dimensional Gaussian function (with FWHM equal to the FWHM of the actual images) to mimic observational effects such as the instrumental point-spread effect and atmospheric seeing. The modeled image is then collapsed into a one-dimensional profile as was done with the observations (Section 2.2). Observed and modeled surface brightness profiles are normalized to three FWHMs beyond the nucleus

Table 2
General Parameters for the Dust Model

Parameter	Value
Semimajor axis a	3.48762 AU
Eccentricity e	0.72017
Inclination i	6°79902
Longitude of the ascending node Ω	13°77506
Argument of perihelion ω	347°55924
Epoch of perihelion passage t_p	2014 Dec 27.05599 UT
Total magnitude H	10.7
Non-grav. radial acceleration parameter A_1	4.075×10^{-9} AU/d ²
Non-grav. transverse acceleration parameter A_2	5.744×10^{-11} AU/d ²
Nucleus radius r_c	0.9 km
Nucleus bulk density ρ_c	500 kg m ⁻³ (assumed)
Dust bulk density ρ_d	1000 kg m ⁻³ (assumed)
Minimum dust size $\beta_{rp,max}$	1.0

Notes. The orbital elements are quoted from the JPL elements K085/15. The nucleus radius is reported by Fernández et al. (2013).

along the Sun-comet axis. We mask out the region within one FWHM from the nucleus to avoid contamination of the signal from the nucleus. The region that is dominated by submicron-sized dust (i.e., the tailward region that is too far from the nucleus for $>1 \mu\text{m}$ dust to reach) is also masked, as we are focused on micron- to millimeter-sized dust. To evaluate the degree of similarity between the observed and the modeled profiles, we calculate the normalized error variance (NEV) as defined by

$$\text{NEV} = \frac{1}{n} \sum_{i=1}^n \frac{\sqrt{(M_i - O_i)^2}}{O_i}, \quad (4)$$

where n is the number of pixels and M_i and O_i are the pixel brightness from the modeled and observed brightness profile, respectively. We set the tolerance level of NEV to 10%. The input parameters, test grids, and best-fit results are tabulated in Tables 2 and 3 and Figure 4, respectively.

It is encouraging that the best-fit models under the respective outburst epochs are largely consistent. We conclude that the characteristic ejection speed $V_0 = 300\text{--}650 \text{ m s}^{-1}$ for the ejecta of the first outburst, while $V_0 = 550\text{--}750 \text{ m s}^{-1}$ for the ejecta of the second outburst. The dust size index is at the range of $q \approx -3.5$. The ejection speed is comparable to or is slightly larger than the one derived from the classic Whipple (1950) model (which gives $V_0 \sim 400 \text{ m s}^{-1}$ in our model), while the size index is comparable to the classic value, $q = -3.6$ (Fulle 2004). It also appears that the characteristic ejection speed of the second outburst is higher than that of the first outburst, which seemingly supports the idea that the second outburst was a more energetic event than the first one.

4. DISCUSSION

4.1. Nature of the Outburst

The total mass of the dust emitted in the two outbursts is related to the effective scattering cross section of the materials, C_e , that can be calculated by

$$C_e = \left(\frac{r_H}{1 \text{ AU}} \right)^2 \frac{\pi \Delta^2}{A_\lambda(\alpha)} 10^{0.4(m_{\odot,\lambda} - m_\lambda)}, \quad (5)$$

where $A_\lambda(\alpha)$, the phase-angle-corrected geometric albedo, is calculated using the compound Henyey–Greenstein model by Marcus (2007), assuming $A_\lambda(0^\circ) = 0.05$, and $m_{\odot,\lambda}$ and m_λ are the apparent magnitudes of the Sun and the comet. This yields $C_e = 7 \times 10^3 \text{ km}^2$ for the first outburst and $C_e = 2 \times 10^4 \text{ km}^2$ for the second outburst, using the photometric measurements in Figure 1. The total mass of the ejecta can then be calculated via $M_d = \frac{4}{3} \rho_d \bar{a}_d C_e$, where the mean dust size \bar{a}_d can be derived from the dust model discussed in Section 3.2. Considering the variances among the best-fit models, we derive $M_d = (2\text{--}3) \times 10^5 \text{ kg}$ for the first outburst and $M_d = (4\text{--}5) \times 10^5 \text{ kg}$ for the second outburst (depending on the exact timing of the individual outburst), corresponding to less than 10^{-7} of the nucleus mass assuming a spherical nucleus.

With this mass, the specific energy of the two outbursts is calculated to be $(0.3\text{--}2) \times 10^5 \text{ J kg}^{-1}$ using the speed component derived from the dust model. This value is comparable to the value derived for 17P/Holmes’s 2007 outburst ($\sim 10^5 \text{ J kg}^{-1}$; see Reach et al. 2010; Li et al. 2011). For the case of 17P/Holmes, the large distance to the Sun at the time of its outburst, as well as the closeness of the derived specific energy to the specific energy of the amorphous ice to crystalline, is compatible with the idea that the comet’s mega-outburst was triggered by the energy released by the crystallization of amorphous ice. However, 15P/Finlay was much closer to the Sun at its two outbursts than 17P/Holmes at its 2007 outburst (1.0 AU versus 2.5 AU), such that solar heat may be sufficient to drive the outburst to some degree; hence, we consider it difficult to assess the role of crystallization for 15P/Finlay’s outburst at this stage.

4.2. The Finlayid Puzzle Revisited

15P/Finlay is puzzling in the sense that despite its occasional proximity to Earth’s orbit, the hypothetical Finlayid meteor shower has never been observed. This matter has been discussed in depth by Beech et al. (1999), who concluded that the perturbation of Jupiter has effectively dispersed the meteoroid stream, such that $\gtrsim 99\%$ of the meteoroids released ~ 20 orbits ago would end up with distant *nodal* passages ($>0.01 \text{ AU}$) from Earth’s orbit. However, we think that this conclusion is unconvincing as the nodal plane approximation for Earth impact may not be valid for 15P/Finlay owing to its shallow orbital plane ($i = 6^\circ.8$). Additionally, new astrometric observations of 15P/Finlay in the past decade have reduced the uncertainty of the orbital elements by an order of magnitude; hence, the issue of the long-term evolution of the Finlayid meteoroid stream is worth revisiting.

We first investigate the orbital stability of 15P/Finlay. This is done by generating 100 clones of 15P/Finlay using the orbital covariance matrix provided in JPL K085/15, and integrating all of them 10^3 yr backward. The integration is performed with MERCURY6 using the Bulirsch–Stoer integrator. The evolution of the perihelion distance of all clones is shown in Figure 5. It can be seen that the perihelion distances of the clones are highly compact until AD 1613, when a close encounter (miss distance of the order of 0.1 AU) between 15P/Finlay and Jupiter occurred. This implies that any backward meteoroid stream simulation will be physically meaningful only as long as the starting date is after AD 1613.

Table 3
Best-fit Dust Models for the FRAM and Vicksburg Observations

	Outburst Epoch (UT)	Observation Epoch (UT)	V_0 (m s^{-1})	q
Test grids	100 to 1200 in steps of 20	-5.4 to -2.0 in steps of 0.1
First Outburst	2014 Dec 15, 10 hr	2014 Dec 17	320 ± 10	-3.7 ± 0.2
	...	2014 Dec 18	320 ± 20	-3.0 ± 0.3
	2014 Dec 16, 0 hr	2014 Dec 17	640 ± 30	-4.0 ± 0.6
	...	2014 Dec 18	670 ± 90	-3.7 ± 0.5
Second Outburst	2015 Jan 15, 12 hr	2015 Jan 18	540 ± 40	-3.6 ± 0.6
	...	2015 Jan 19	590 ± 120	-3.4 ± 0.5
	...	2015 Jan 21	570 ± 30	-3.6 ± 0.6
	2015 Jan. 16, 0 hr	2015 Jan 18	780 ± 30	-3.8 ± 0.5
	...	2015 Jan 19	670 ± 100	-3.6 ± 0.5
	...	2015 Jan 21	750 ± 40	-3.4 ± 0.4

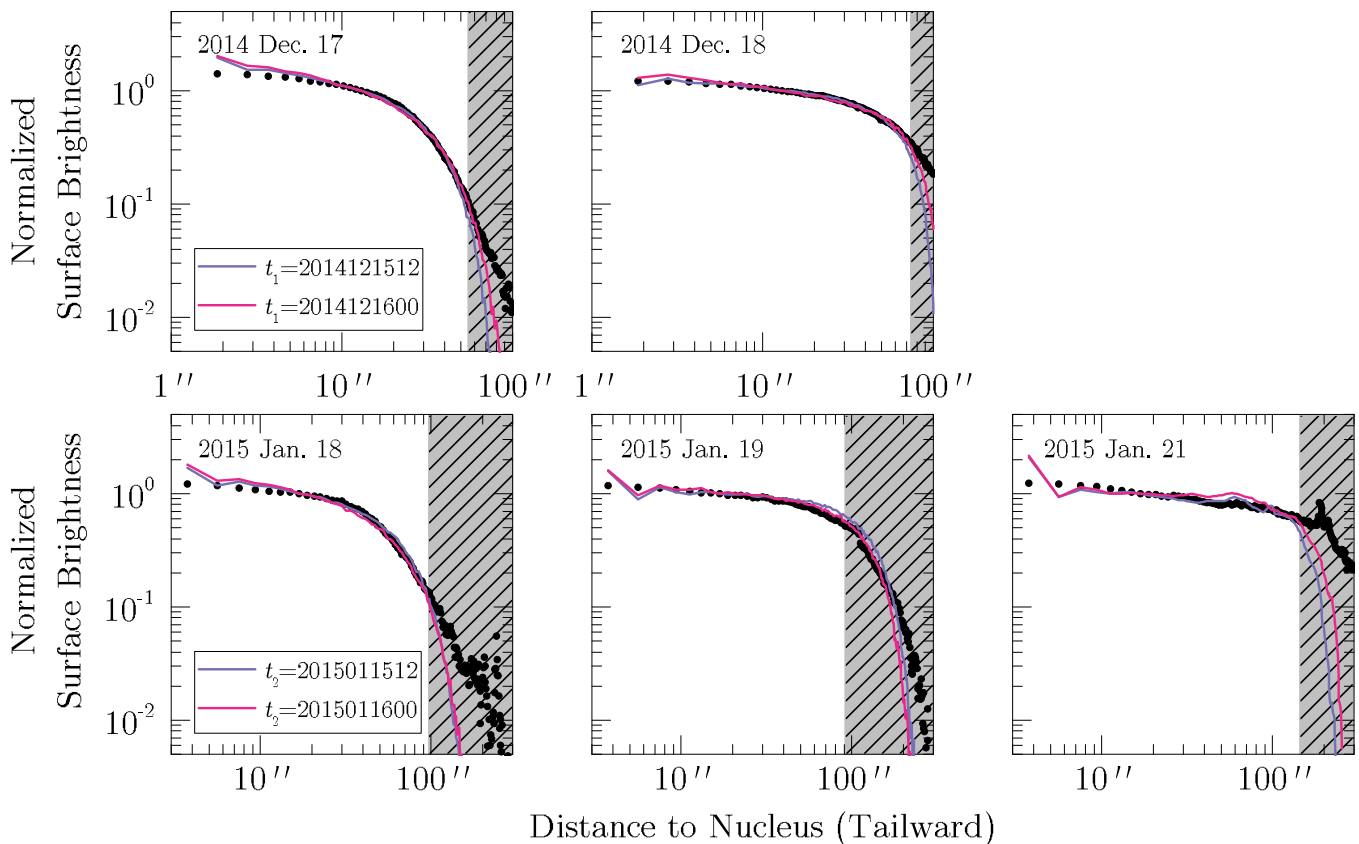


Figure 4. Observed surface brightness profiles (scatter dots) and the best-fit dust models (color lines) for FRAM and Vicksburg observations. The assumed outburst epochs (see main text) are denoted as t_1 for the first outburst and t_2 for the second outburst. The regions that are dominated by submicron-sized particles are masked from modeling as described in the main text. For the profile on 2015 January 19 an additional region is masked owing to the contamination of a background star.

Next, we simulate a total of 39,000 (a randomly chosen number) hypothetical particles released by 15P/Finlay during its 1886, 1909, and 1960 perihelion passages and examine their distribution in 2001, to directly compare to the Beech et al. (1999) simulations. The simulation is performed using the same collection of subroutines described in Section 3.2 except that the ejection model by Crifo & Rodionov (1997) is used and only $\beta = 0.001$ (millimeter-sized) particles are simulated. The MOID vector \mathbf{MOID} between Earth and each meteoroid is calculated using the subroutine developed by Gronchi (2005) to assess the likelihood of an Earth encounter. The original MOID

is defined as a scalar; here I define the direction of \mathbf{MOID} to be the same as $r_D - r_E$, where r_D and r_E are the heliocentric distance of the meteoroid and Earth, respectively, at the MOID point. We find that as much as $\sim 15\%$ of the particles stay within 0.01 AU of Earth's orbit as of 2001, different from the finding of Beech et al. (1999). In addition, the dust trail is able to overlap with Earth's orbit (Figure 6), further supporting the idea that a significant number of particles released by 15P/Finlay 10–20 orbits ago may still have direct encounters with Earth.

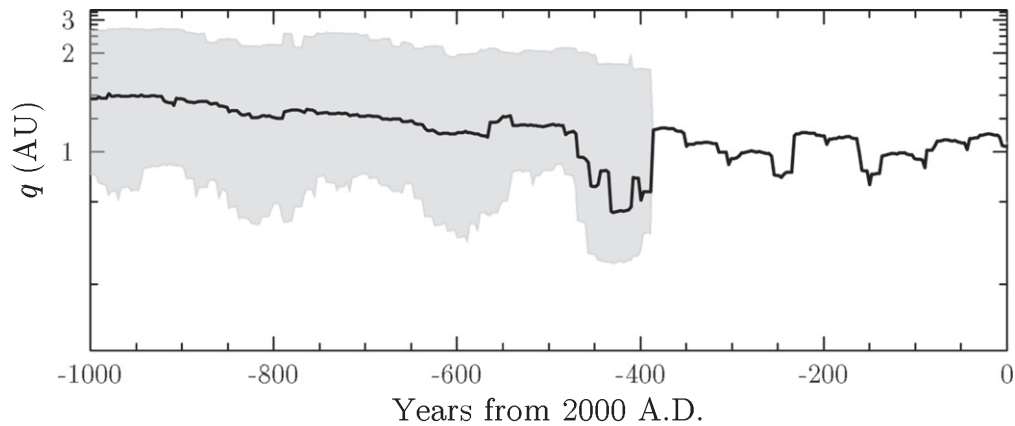


Figure 5. Dynamical evolution of the perihelion distance of 100 clones of 15P/Finlay in the interval of AD 1000–2000.

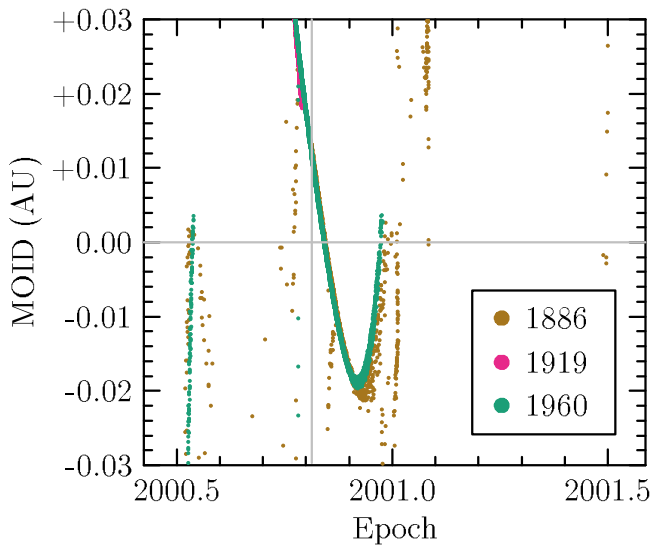


Figure 6. Distribution of the dust trails released by 15P/Finlay during its 1886, 1909, and 1960 perihelion passages in 2001. The vertical gray line marks the time at which Earth passes the trails. It can be seen that the trails cross Earth’s orbit, suggestive of the possibility of a direct encounter to Earth.

The background meteoroid flux originating from 15P/Finlay may be estimated in an order-of-magnitude manner. The absolute magnitude of 15P/Finlay is ~ 100 times brighter than low-activity comet 209P/LINEAR, for which the meteoroid production capacity has been measured to be 10^{14} meteoroids per orbit (Ye et al. 2016). Hence, in 10 orbits, 15P/Finlay would generate 10^{17} meteoroids. Assuming that the meteoroids distribute uniformly along the orbit with an orbital period of 5 yr, as well as a delivery efficiency of 10% to the region ± 0.01 AU from Earth’s orbit and a characteristic duration of meteor activity of 1 week, the flux can be calculated by $10^{17} \times 10\% \times 7 \text{ days}/5 \text{ yr} \approx 0.1 \text{ km}^{-2} \text{ hr}^{-1}$, which should be detectable by modern meteor survey systems.

To look for any undetected Finlayid activity, we conduct a “cued” search in the Canadian Meteor Orbit Radar (CMOR) database. CMOR is an interferometric radar array located near London, Ontario, operating at 29.85 MHz with a pulse repetition frequency of 532 Hz (see Jones et al. 2005; Brown et al. 2008; Ye et al. 2013). Since its commission in 2002, CMOR has measured 12 million meteoroid orbits, making it suitable for the search for weak meteor showers such as the

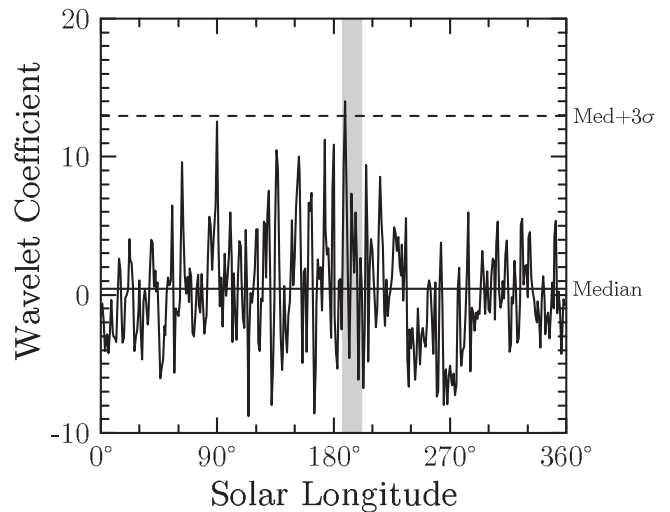


Figure 7. Variation of the wavelet coefficient at the calculated Finlayid radiant $\lambda - \lambda_{\odot} = 66^{\circ}$, $\beta = -25^{\circ}$, $v_G = 13 \text{ km s}^{-1}$ using the stacked “virtual year” CMOR data. The shaded area is the expected time window for Finlayid activity (solar longitude $\lambda_{\odot} \sim 193^{\circ}$).

Finlayids. We first calculate the characteristics of the hypothetical Finlayid radiant using the simulation results above, which yields $\lambda - \lambda_{\odot} = 66^{\circ} \pm 11^{\circ}$, $\beta = -18^{\circ} \pm 9^{\circ}$ at Sun-centered ecliptic coordinates, and a geocentric speed of $13 \pm 3 \text{ km s}^{-1}$. We then combine 14 yr of CMOR data into a stacked “virtual” year and look for any enhanced activity at the location of the theoretical radiant, using a wavelet-based search algorithm (Brown et al. 2008, 2010) with probe sizes tuned to the expected radiant characteristics (radiant probe size $\sigma_{\text{rad}} = 10^{\circ}$, velocity probe size $\sigma_v = 3 \text{ km s}^{-1}$).

As shown in Figure 7, no significant enhancement can be found at the expected period of activity (solar longitude $\lambda_{\odot} \sim 210^{\circ}$). Ye et al. (2016) have calculated that the detection limit for the wavelet algorithm applied on CMOR is at the order of $0.01 \text{ km}^{-2} \text{ hr}^{-1}$; however, CMOR sensitivity is also an order of magnitude less at a southerly radiant at $\delta = -40^{\circ}$ comparing to northerly radiants, so the shower flux limit is probably closer to $0.1 \text{ km}^{-2} \text{ hr}^{-1}$. Hence, the existence and intensity (or derived upper limit) of the Finlayid meteor shower are not definitive, but they favor southern hemisphere meteor surveys (e.g., Younger et al. 2012; Janches et al. 2013).

Table 4
Predictions of the 2021 Encounter of 15P/Finlay’s 2014 Meteoroid Trails

Reference	Peak Time (UT)	Radiant (α_g, δ_g)	v_g (km s $^{-1}$)	Note
Maslov ^a	2021 Oct 7, 1:19	255°8, −48°3	10.7	ZHR 5–50
Sato ^b	2021 Oct 7, 1:10	255°7, −48°4	10.7	...
Vaubailon ^c	No encounter
This work	2021 Oct 7, 0:34–1:09 ^d	255°6, −48°4	10.7	Ejecta from the first outburst
	2021 Oct 6, 21:59–22:33 ^e	256°3, −48°5	10.7	Ejecta from the second outburst

Notes.

^a <http://feraj.narod.ru/Radiants/Predictions/1901-2100eng/Finlayids1901-2100predeng.html>, retrieved 2015 March 4.

^b <https://groups.yahoo.com/neo/groups/meteorobs/conversations/messages/44030>, retrieved 2015 March 4.

^c <https://groups.yahoo.com/neo/groups/meteorobs/conversations/messages/44035>, retrieved 2015 March 4.

^d The peak time of 0:34 corresponds to the assumed outburst epoch of 2014 December 15.4 UT, while 1:09 corresponds to the assumed outburst epoch of 2014 December 16.0 UT.

^e The peak time of 21:59 corresponds to the assumed outburst epoch of 2015 January 16.0 UT, while 22:33 corresponds to the assumed outburst epoch of 2015 January 15.5 UT.

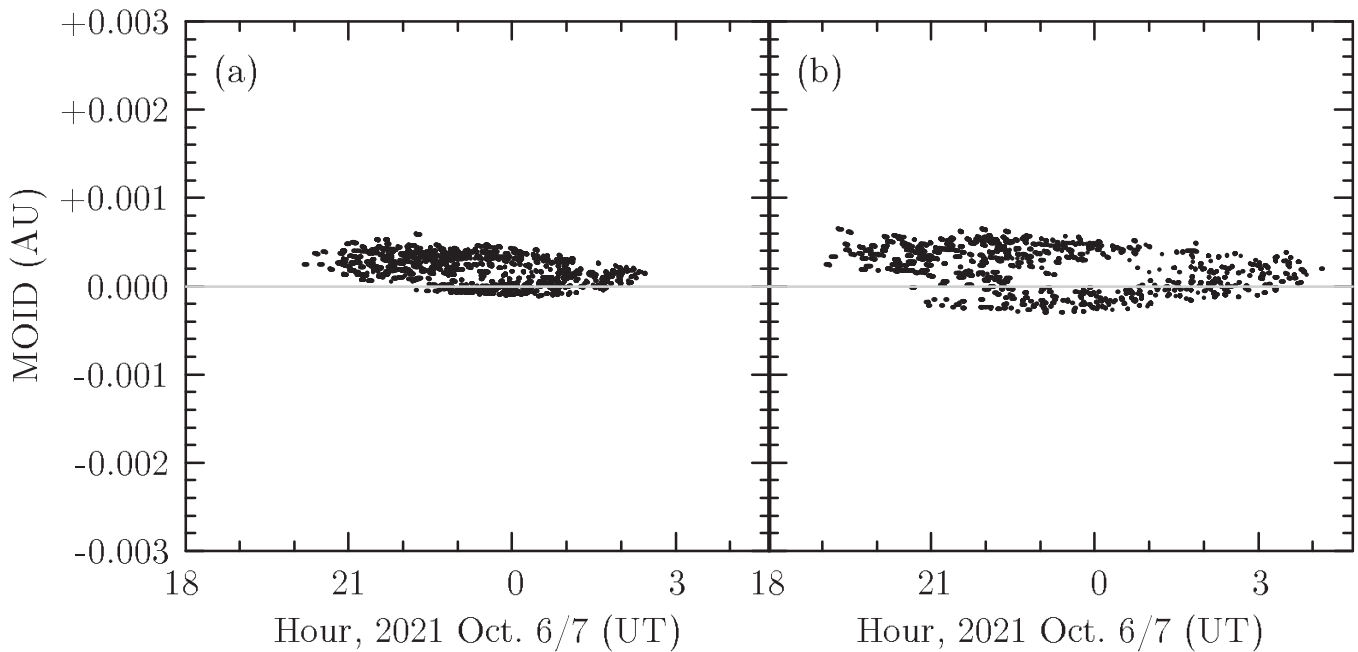


Figure 8. Encounter of 15P/Finlay’s 2014/2015 outburst ejecta in 2021 October 6/7. Panel (a) gives the simulation results assuming the earliest possible outburst epoch (2014 December 15.4 UT for the first outburst, 2015 January 15.5 UT for the second outburst), while panel (b) gives the results assuming the latest possible outburst epoch (2014 December 16.0 UT for the first outburst, 2015 January 16.0 UT for the second outburst).

4.3. The 2021 Earth Encounter of the 2014/2015 Outburst Ejecta

The potential 2021 encounter with the 2014 trail from 15P/Finlay is of particular interest given the additional dust released from the two outbursts, as it offers an excellent opportunity to examine 15P/Finlay’s ejecta. The encounter is studied by simply extending the numerical integration described in Section 3.2 to the year of 2021. Similar to the meteoroid trail model presented in Ye et al. (2016), we assigned a *space criterion* to select Earth-approaching meteoroids, defined by

$$\Delta X = v_{\text{rel}} \times \Delta T, \quad (6)$$

where v_{rel} is the relative velocity between the meteoroid and Earth and ΔT is called the *time criterion*, which is the characteristic duration of the event, typically $\Delta T = 1$ day. Similar to the dust model discussed in Section 3.2, we test two

sets of outburst epochs that correspond to either the epochs of the last non-outburst report or the first positive report.

The simulation result confirms the general findings by Maslov and Sato, that a direct encounter of the 2014/2015 meteoroid trail will occur on 2021 October 6/7 (Table 4, Figure 8) with an FWHM of about 1 hr. The uncertainty in outburst epochs results in about 0.5 hr uncertainty in the peak time in 2021. The ejecta from the second outburst are calculated to arrive around 2021 October 6 at 22 hr UT, followed by those from the first outburst, which are expected to arrive around 2021 October 7 at 1 hr UT. The radiant is at geocentric equatorial coordinates of $\alpha_G = 257^\circ$, $\delta_G = -48^\circ$ or in the constellation of Ara, favoring the observers in the southern tip of Africa. As 15P/Finlay was ~ 20 times more active during the two outbursts compared to its normal dust production level as indicated by Figure 1, the meteor activity may also be significantly stronger than previously expected.

However, we also note that the range of the meteoroid sizes delivered to Earth's vicinity seems to be concentrated at the order of $\beta \sim 0.001$, which translates to a visual magnitude of +8 (Campbell-Brown & Koschny 2004) considering the very low encounter speed. This indicates that the meteor activity in 2021 may only be visible to meteor radars and low-light video cameras.

5. SUMMARY

We present an analysis of the two outbursts of the potential CATO, 15P/Finlay, at its 2014/2015 perihelion passage. These outbursts took place between 2014 December 15.4–16.0 UT and 2015 January 15.5–16.0 UT as constrained by ground-based and spacecraft observations. As seen in monitoring images, both outbursts produced a newly formed dust shell that expands and fades in ~ 1 week.

The images from five observing nights (two for the first outburst, three for the second outburst) were studied using a Monte Carlo dust model and yield a characteristic ejection speed of $V_0 = 300\text{--}650 \text{ m s}^{-1}$ for the ejecta of the first outburst and $V_0 = 550\text{--}750 \text{ m s}^{-1}$ for that of the second outburst, taking into account the uncertainty in the determination of outburst epoch. The dust size index is in the range of $q \approx -3.5$. We derive the mass of the ejecta to be $M_d = (2\text{--}3) \times 10^5 \text{ kg}$ for the first outburst and $M_d = (4\text{--}5) \times 10^5 \text{ kg}$ for the second outburst, corresponding to less than 10^{-7} of the nucleus mass. The specific energy of the two outbursts is calculated to be $(0.3\text{--}2) \times 10^5 \text{ J kg}^{-1}$, comparable to the specific energy produced by the crystallization of amorphous ice, but does not prove the latter as the driving force for 15P/Finlay's outbursts.

We also revisited the long-standing puzzle of the nondetection of the Finlayids, the hypothetical meteor shower generated by 15P/Finlay, as well as the future possibility for meteor activity generated by the 2014/2015 outbursts. We find that the efficiency of meteoroid delivery to Earth's orbit is ~ 10 times higher than previously reported by Beech et al. (1999). Assuming that 15P/Finlay's recent (last ~ 20 orbits) activity is comparable to its contemporary level, the meteoroid flux of the Finlayids should be high enough to be detected by modern meteor surveys. However, a cued search with the 12 million meteor orbits gathered by the CMOR over the past 13 yr does not reveal any positive detection. The encounter with the 2014/2015 outburst ejecta may provide an answer to the Finlayid puzzle, as Earth is expected to pass through the ejecta trails directly between 2021 October 6 at 22 hr UT and October 7 at 1 hr UT, with a chance for some significant meteor activity in the video or radio range. The timing and the southerly radiant in the constellation of Ara will favor observers in the southern tip of Africa.

The recent outburst episode of 15P/Finlay seems to suggest that the comet, originally thought to be quiet and largely inactive, does possess the ability for significant activity. Whether the recent outbursts are the overtures of a resurrection of the comet or a finale of its career remains to be seen. Cometary observations in the forthcoming perihelion passage in 2021 July, as well as observations during the potential meteor outburst, will likely provide more information.

We thank an anonymous referee for his/her comments. We also thank Paul Wiegert for permission to use his computational resource, Margaret Campbell-Brown for her meteoroid ablation code, and Zbigniew Krzeminski, Jason Gill, Robert Weryk, and Daniel Wong for helping with CMOR operations. The operation of the robotic telescope FRAM is supported by the EU grant GLORIA (No. 283783 in FP7-Capacities program) and by the grant of the Ministry of Education of the Czech Republic (MSMT-CR LG13007). Funding support from the NASA Meteoroid Environment Office (cooperative agreement NNX11AB76A) for CMOR operations is gratefully acknowledged. This work would not be possible without the inputs from the amateur community, and their contributions are gratefully acknowledged.

REFERENCES

- Beech, M., Nikolova, S., & Jones, J. 1999, *MNRAS*, **310**, 168
 Bertaux, J. L., Kyrölä, E., Quémerais, E., et al. 1995, *SoPh*, **162**, 403
 Brown, P., Weryk, R. J., Wong, D. K., & Jones, J. 2008, *Icar*, **195**, 317
 Brown, P., Wong, D. K., Weryk, R. J., & Wiegert, P. 2010, *Icar*, **207**, 66
 Buzzi, L., Muler, G., Kidger, M., et al. 2007, *IAUC*, **8886**, 1
 Campbell-Brown, M. D., & Koschny, D. 2004, *A&A*, **418**, 751
 Chambers, J. E. 1999, *MNRAS*, **304**, 793
 Crifo, J. F., & Rodionov, A. V. 1997, *Icar*, **127**, 319
 Everhart, E. 1967, *AJ*, **72**, 716
 Everhart, E. 1985, in Proc. IAU Coll. 83, Dynamics of Comets: Their Origin and Evolution, Vol. 115, ed. A. Carusi & G. B. Valsecchi (Dordrecht: Reidel), 185
 Fernández, J. A., & Sosa, A. 2015, *IAUGA*, **22**, 44024
 Fernández, Y. R., Kelley, M. S., Lamy, P. L., et al. 2013, *Icar*, **226**, 1138
 Fulle, M. 2004, in Motion of Cometary Dust, ed. M. C. Festou, H. U. Keller & H. A. Weaver (Tucson, AZ: Univ. Arizona Press), 565
 Gombosi, T. I., Nagy, A. F., & Cravens, T. E. 1986, *RvGeo*, **24**, 667
 Gronchi, G. F. 2005, *CeMDA*, **93**, 295
 Henden, A. A., Levine, S. E., Terrell, D., Smith, T. C., & Welch, D. 2012, *JAVSO*, **40**, 430
 Ishiguro, M., Ham, J.-B., Tholen, D. J., et al. 2011, *ApJ*, **726**, 101
 Ishiguro, M., Jewitt, D., Hanayama, H., et al. 2014, *ApJ*, **787**, 55
 Janches, D., Hormaechea, J. L., Brunini, C., Hocking, W., & Fritts, D. C. 2013, *Icar*, **223**, 677
 Jewitt, D. 2012, *AJ*, **143**, 66
 Jewitt, D., Ishiguro, M., Weaver, H., et al. 2014, *AJ*, **147**, 117
 Jones, J., Brown, P., Ellis, K. J., et al. 2005, *P&SS*, **53**, 413
 Kresak, L., & Kresakova, M. 1989, *BAICz*, **40**, 269
 Kronk, G. W. 2004, *Cometography* (Cambridge: Cambridge Univ. Press)
 Kronk, G. W. 2008, *Cometography* (Cambridge: Cambridge Univ. Press)
 Kronk, G. W., & Meyer, M. 2010, *Cometography: A Catalog of Comets*, Vol. 5 (Cambridge: Cambridge Univ. Press)
 Li, J., Jewitt, D., Clover, J. M., & Jackson, B. V. 2011, *ApJ*, **728**, 31
 Licandro, J., Campins, H., Mothé-Diniz, T., Pinilla-Alonso, N., & de León, J. 2007, *A&A*, **461**, 751
 Marcus, J. N. 2007, *ICQ*, **29**, 39
 Meech, K. J., & Belton, M. J. S. 1989, *IAUC*, **4770**, 1
 Mommert, M., Hora, J. L., Harris, A. W., et al. 2014, *ApJ*, **781**, 25
 Reach, W. T., Vaubaillon, J., Lisse, C. M., Holloway, M., & Rho, J. 2010, *Icar*, **208**, 276
 Tancredi, G. 2014, *Icar*, **234**, 66
 Whipple, F. L. 1950, *ApJ*, **111**, 375
 Wyatt, S. P., & Whipple, F. L. 1950, *ApJ*, **111**, 134
 Ye, Q., Brown, P. G., Campbell-Brown, M. D., & Weryk, R. J. 2013, *MNRAS*, **436**, 675
 Ye, Q., & Wiegert, P. A. 2014, *MNRAS*, **437**, 3283
 Ye, Q.-Z., & Hui, M.-T. 2014, *ApJ*, **787**, 115
 Ye, Q.-Z., Hui, M.-T., Brown, P. G., et al. 2016, *Icar*, **264**, 48
 Younger, J. P., Reid, I. M., Vincent, R. A., & Murphy, D. J. 2012, *MNRAS*, **425**, 1473
 Zacharias, N., Finch, C. T., Girard, T. M., et al. 2013, *AJ*, **145**, 44